INTERNATIONAL JOURNAL OF HYDROGEN ENERGY 42 (2017) 1203–1211

Available online at www.sciencedirect.com

ScienceDirect

journal homepage: www.elsevier.com/locate/he

A 2D and 3D X-ray μ-diffraction and μ-fluorescence study of a mixed ionic electronic conductor

Dario Ferreira Sanchez [a,*], *Daniel Grolimund* [a], *Maxime Hubert* [b,c], *Pierre Bleuet* [b,d], *Jérôme Laurencin* [b,c]

[a] *Swiss Light Source, Paul Scherrer Institut, CH-5232 Villigen PSI, Switzerland*
[b] *Univ. Grenoble Alpes, F-38000 Grenoble, France*
[c] *CEA/Liten, MINATEC Campus, 17 rue des Martyrs, 38054 Grenoble Cedex 9, France*
[d] *CEA/LETI, MINATEC Campus, F-38054 Grenoble, France*

ARTICLE INFO

Article history:
Received 14 July 2016
Received in revised form
31 October 2016
Accepted 13 November 2016
Available online 6 December 2016

Keywords:
Solid oxide fuel cell
X-ray diffraction tomography
X-ray fluorescence tomography
X-ray micro beam

ABSTRACT

Due to the mixed ionic electronic conductive properties of the Lanthanum Strontium Cobalt Ferrite (LSCF) $La_{0.6}Sr_{0.4}Co_{0.2}Fe_{0.8}O_{3-\delta}$ compound, it is of great scientific and technological interest. Especially in the Solid Oxide Fuel Cell (SOFC) technology, this compound has receiving great attention as a cathode material. However, its chemical reactivity with the Yttria-stabilized Zirconia (YSZ) electrolyte still remains one of the main challenges, which demands a comprehension in the μm and sub-μm range. In order to address the reactivity issues locally in the micrometre scale range, 2D and 3D X-ray μ-diffraction and μ-fluorescence analysis have been performed on a pristine LSCF cathode layer. The cathode was deposited on a dense YSZ electrolyte substrate spaced by a thin Gadolinium doped Ceria Oxide (CGO) barrier layer in between LSCF and YSZ to limit the reactivity. The present approach offers a larger field of view in comparison to electron microscopy techniques. The method can provide a more representative information and may offer some insights on the reactivity distribution along the interfaces. The formation of micro $SrZrO_3$ inclusions in LSCF layer is then indubitably identified, as well as in the CGO/YSZ interface.

Introduction

Solid Oxide Fuel Cells (SOFCs) are of great technological interest owing to their efficiency in converting a wide variety of hydrocarbon fuels and hydrogen to electricity, this route being of higher efficiency and more environmentally benign than a combustion process. There are several challenges involved in the development of this technology. The combination of high operating temperatures and mismatch between the thermal expansion coefficients of the cell components can induce residual stresses. Besides, species interdiffusion between the cell materials can lead to detrimental chemical reactions. The understanding of these phenomena is essential to design innovative solutions such as new alternative materials, and overcome the SOFC technology challenges by extending devices lifetime and reliability. In this context, the development of standard methodologies to investigate the SOFCs local structure and chemical/elemental composition in the micrometre range is critical.

To address these SOFCs issues, X-ray imaging techniques have been demonstrated by several authors to be among the most suitable ones. Among their advantages, it can be mentioned (i) the potential to perform in situ experiments [40];

* *Corresponding author.*
E-mail addresses: dario.f.sanchez@gmail.com, dario.ferreira@psi.ch (D.F. Sanchez).
http://dx.doi.org/10.1016/j.ijhydene.2016.11.094

(ii) the resolution that can be achieved down to the tens of nanometres [8,38]; (iii) the capability to probe about tens of micrometres within the matter and (iv) the ability to get depth resolved crystalline contrast by analysing the X-ray diffraction (XRD) [37] and chemical–elemental contrast by analysing the X-ray fluorescence (XRF) [4]. A great number of X-ray imaging techniques have been developed and applied in the last recent years, which can be divided basically in two different categories: full-field and scanning (in μm, sub-μm and nm scale). Among the main advantages of the full-field techniques, it can be highlighted the capability to perform high speed 3D measurements. However, X-ray scanning techniques may be of great interest for the relatively reduced analysis complexity and the capability to perform multimodal analysis, e.g. simultaneous XRD and XRF analysis. Several examples of successful applications of the combination of μ-XRD and μ-XRF tomography can be found in the literature [1–4,28]. This combination is of particular interest for the investigation of SOFCs, since the correlation between the chemical–elemental spatial distribution and the crystalline structure is crucial for understanding the mechanisms and properties evolved in the SOFCs operation.

In the real SOFCs systems, processes at the cathode-metallic interconnect interface, such as chromium poisoning, are major contributors to the overall cell degradation [13,20,30,48]. Here, we focused on the intrinsic degradation mechanisms of a particular cathode: the Lanthanum Strontium Cobalt Ferrite (LSCF). In the current state of the art in SOFC science and technology, Lanthanum Strontium Cobalt (LSC) oxide and LSCF oxide cathodes are been preferable over the standard/largely employed Lanthanum Strontium Manganite (LSM) with Yttria Stabilized Zirconia (YSZ), LSM/YSZ. Both LSCF and LSC materials presents much higher electrochemical performances than the classical LSM/YSZ composite. Indeed LSC and LSCF exhibit a mixed ionic electronic conductivity (MIEC), so that the oxygen reduction takes on all the surface area of the electrodes [26]; whereas the electrochemical reactions are restricted to the LSM/YSZ/pore triple phase boundary (TPB) lengths. However, the chemical instability of LSC and LSCF may limit their working time [9,11,12,15,29,35,48]. Their high reactivity with the YSZ electrolyte may lead to the formation of secondary oxides phases, such as $SrZrO_3$ and/or $La_2Zr_2O_7$, which decreases the device's performance due to the lower ionic conductivity and higher mismatch of thermal expansion coefficient (TEC) with respect to the LSCF surrounding components [6,17,27,43,49]. In order to prevent the reactivity with YSZ electrolyte to form undesired secondary phases, a gadolinium-doped ceria oxide (CGO) diffusion barrier is commonly used as an interlayer in between LSCF and YSZ [21,22,31,32,45]. CGO exhibits purely an ionic conductivity. Also, it exhibits a higher oxygen ionic conductivity at low temperatures and a better chemical compatibility with the electrode materials [14,19,47].

Moreover, TEC mismatches between LSCF and YSZ can cause stress which could lead to a fracture (TEC of $La_{0.6}Sr_{0.4}Fe_{0.8}Co_{0.2}O_{3-\delta}$ is equal to $\approx 17.5 \times 10^{-6}$ K^{-1} whereas the one for Zirconia stabilised with 8 mol% of yttrium oxide (8YSZ) is $\approx 10.5 \times 10^{-6}$ K^{-1}). Manufacturing processes and several thermal cycles in operation can also lead to the electrode mechanical degradation [25]. To minimize this problem, a composite made of LSCF and CGO was proposed.

In the in the μm and sub-μm scale range, the correlation between the Sr diffusion and the formation of the crystalline phase $SrZrO_3$ due to degradation processes have been reported in the literature only based on the identification of Sr element spatial distribution, detected by means of XRF, energy dispersive X-ray spectroscopy (EDX) and high-angle annular dark-field scanning transmission electron microscopy (HAADF-STEM) [7,21,31,36,46]. However, from our best knowledge, no direct crystalline identification by using a diffraction technique has been reported for SOFCs. The formation of the $SrZrO_3$ crystalline phase has been only identified in powder mixtures (macroscopical analysis) of LSM + YSZ and LSCF + YSZ, through the utilization of X-ray diffractograms in Refs. [6,32]. Here, in order to address these reactivity issues locally in the micrometre scale range, a 2D and 3D X-ray μ-diffraction and μ-fluorescence study has been performed on a pristine LSCF cathode layer. The cathode was deposited on a thin Gadolinium doped Ceria Oxide (CGO) layer which is on a dense YSZ electrolyte substrate. Particularly, in comparison with electron microscopy techniques the present approach offer a larger field of view, which can provide a more representative information and some insights on the distribution of reactivity along the interfaces. The formation of micro $SrZrO_3$ inclusions in LSCF layer is then indubitably identified, as well as in the CGO/YSZ interface.

Experimental

The sample is a 23 μm thick electrode layer of a commercial $La_{0.6}Sr_{0.4}Co_{0.2}Fe_{0.8}O_{3-\delta}$ (LSCF) single phase electrode, deposited on a 2 μm thin protective interlayer of gadolinium doped ceria $Gd_{0.1}Ce_{0.9}O_{2-\delta}$ (CGO), which limits the reactivity of LSCF with the dense 8YSZ electrolyte substrate. Since the sample is constituted by relatively heavy elements, e.g. Y and Zr, with a high mass density, the X-ray attenuation length is of only about several tens of micrometres considering the photons energy used in the present work. For this reason, in order to obtain a sample with a lateral size of about 40 μm, the sample was prepared through the standard Focused Ion Beam (FIB) lift-out technique [5,39], with plasma FIB using Xe^+ ions. This process allows to obtain a sample with an axisymmetric geometry suitable for the X-ray tomography experiments. The sample was fixed on an aluminium tip, to be later mounted on a rotational stage for performing the tomography experiments. A scanning electron microscopy (SEM) image in backscattering (BS) mode of the final sample is shown in Fig. 1, where the LSCF and CGO layers and the dense 8YSZ substrate are indicated. The Pt layer is deposited on the surface of the sample before the Xe^+ etching procedure in order to protect from sputtering the original features of LSCF.

The simultaneously μ-beam diffraction (μXRD) and fluorescence (μXRF) experiments (tomography and 2D-raster scan) were carried out at the microXAS beamline at the Swiss Light Source (SLS) synchrotron. The incident pencil beam was focused with a Kirkpatrick–Baez (KB) mirror system to a size of about 1.5 × 1.0 (H × V) μm^2, with the energy of 17.3 keV. The diffraction pattern of a standard polycrystalline sample of Al_2O_3 was used to calibrate the PILATUS 100K detector position with respect to the sample. The measured diffraction

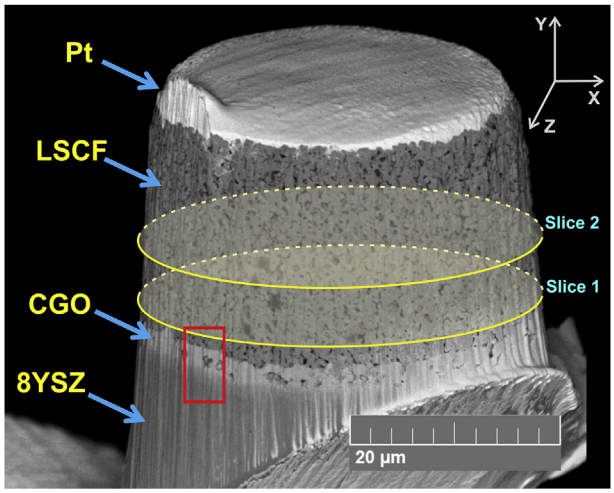

Fig. 1 – Scanning electron microscopy (SEM) image of the investigated sample in this work, in backscattering (BS) mode. The two analysed slice through the tomography experiments are indicated (yellow circles), as well as the 8YSZ/CGO/LSCF interfaces region which is later analysed in more details (red rectangle). In detail in the top right, the sample coordinates referred in this article: the sample high Y direction and sample X and Z lateral directions. (For interpretation of the references to colour in this figure legend, the reader is referred to the web version of this article.)

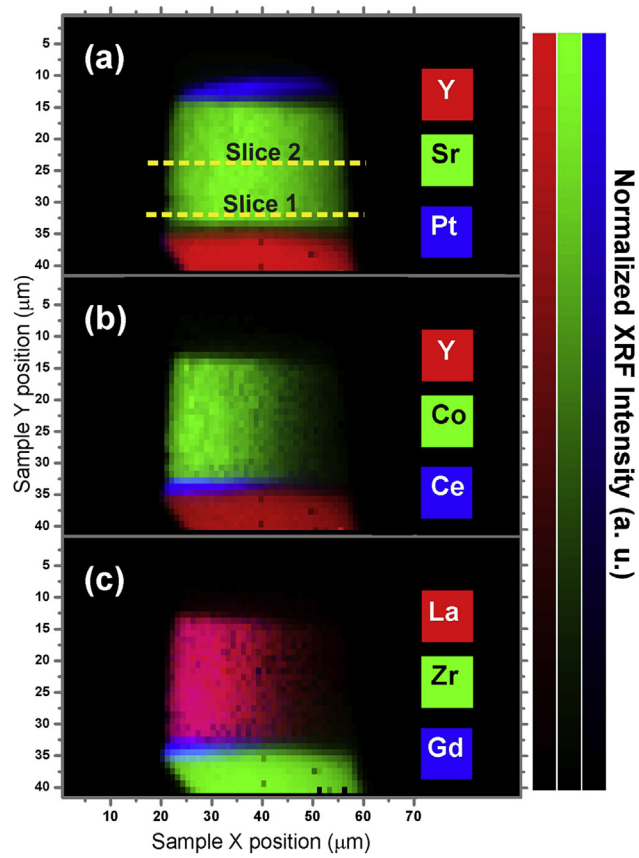

Fig. 2 – (a–c) The chemical–elemental cartographies of La, Pt, Gd, Ce, Zr, Sr, Y and Co obtained from PyMCA analysis of the XRF spectra measured at 18.15 keV. The location of the two slices scanned tomographically, *slice1* and *slice2*, are indicated in (a).

patterns images in the LSCF region resulted in powder rings data, which were then azimuthal by using the software XRDUA [34]. To calibrate sample-detector relative position with respect to the incoming μ-beam direction, the XRD pattern of a well characterised crystalline material of Al_2O_3 was used. In addition, a 2D scanning μXRF experiment was performed with slightly different experimental conditions, that is to say by focussing the beam down to about 1×1 μm^2, with the energy of 18.15 keV (above the Zr absorption edge). The free available software PyMCA developed at the European Synchrotron Radiation Facility [42], was used for the XRF analysis, which allows interactive and as well as batch processing of large data sets.

Results and discussions

Two-dimensional μ-beam sample scanning experiments were performed, with the positions recorded by steps in both the horizontal and vertical directions of 1 by 1 μm, covering an area of 70×41 μm^2. Both the XRD patterns and XRF spectra were recorded at each position at 17.3 keV, and the XRF spectra only at 18.15 keV. The chemical–elemental cartographies of Zr, Y, La, Sr, Gd, Co, Ce and Pt obtained from the μXRF experiment at 18.15 keV are shown in Fig. 2a–c, respectively.

The powder-XRD pattern shown in Fig. 3 is an average pattern over the whole 2D scanned area, which includes not only the LSCF region, but also the Pt and CGO layers, and the 8YSZ substrate. In this pattern, six selected diffracted intensities at a given diffracted angle are indicated, which are called: CGO (reflection (111) of CGO); LSCF′ (reflections (110) and (104) of LSCF); YSZ (reflection (220) of cubic YSZ and reflections (002) and (112) of tetragonal YSZ); $SrZrO_3$ (reflection (121) of $SrZrO_3$); LSCF″ and LSCF‴ (reflections (410), (324), (318) and (1 1 12) of LSCF) – LSCF″ corresponding the lower angle diffraction tail peak and LSCF‴ corresponding central part of the peak.

In Fig. 4a–d, the XRD cartographies are shown, where each image corresponds to four of these diffracted intensity positions: LSCF′, $SrZrO_3$, LSCF″ and LSCF‴.

The tomography experiments were carried out by recording simultaneously both the XRD patterns and XRF spectra at 70 sample positions in the X direction, in steps of 1 μm, and at 180 sample orientations equally spaced by 2°. As depicted in Fig. 1, two slices were scanned in the LSCF region, parallel to the LSCF/CGO interface: one slice of about 2–3 μm above the LSCF/CGO interface, and a second one spaced by 10 μm with respect to the first one. It can be noticed that second slice is located in the central part of the LSCF layer. The two slices are referred in this work as *slice1* and *slice2*, respectively, and their locations are indicated in Figs. 1 and 2a.

For each XRF intensity, a sinogram is built. About 1600 sinograms are then acquired for each XRF intensity in the range of about from 2 to 18 keV. More details of the technique

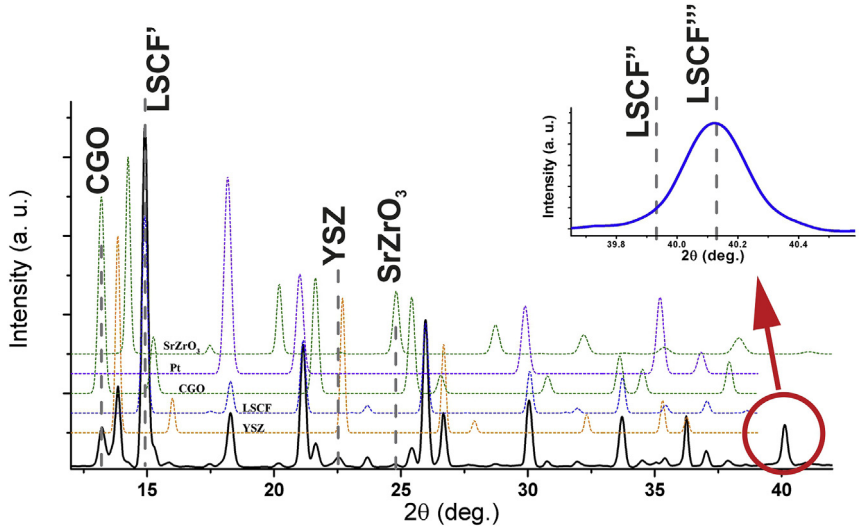

Fig. 3 – Average powder-XRD pattern (black line) over the whole 2D scanned area (LSCF, CGO, 8YSZ and Pt layers), as well as the fitted patterns of the individual phases, namely the $SrZrO_3$, Pt, CGO, LSCF and YSZ. Also, some regions of interest are marked (named CGO, LSCF′, YSZ, $SrZrO_3$, LSCF″ and LSCF‴), which are later discussed in Fig. 4.

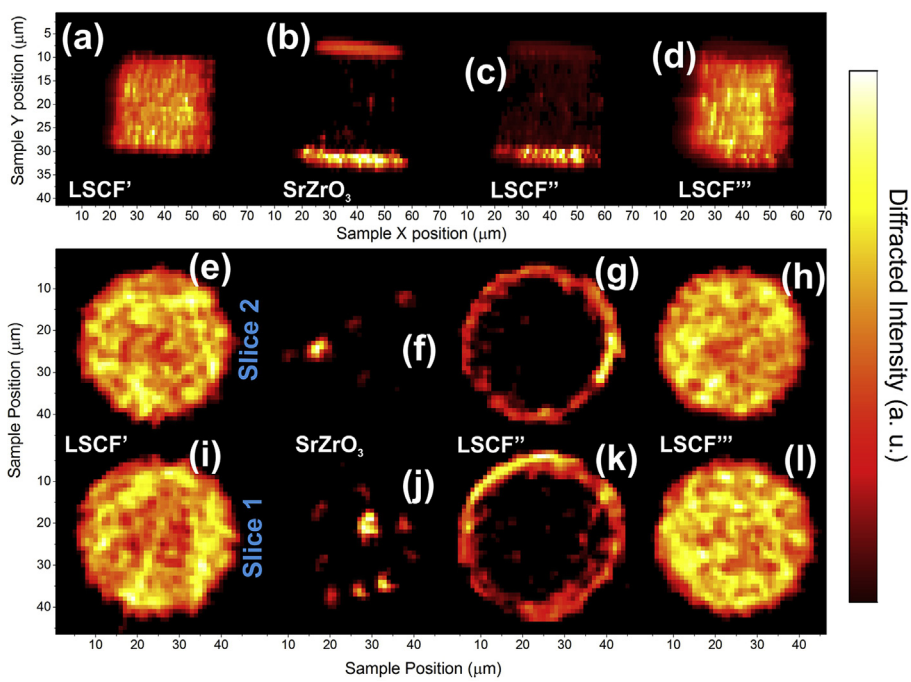

Fig. 4 – (a–b) XRD cartographies obtained from the region of interest LSCF′, $SrZrO_3$, LSCF″ and LSCF‴; each one corresponds to a given diffracted intensity at a corresponding diffracted angle which are respectively indicated with a dashed grey line in Fig. 3. XRD tomographic reconstructions for the layers *slice1* (i–l) and *slice2* (e–h) are shown, also for LSCF′, $SrZrO_3$, LSCF″ and LSCF‴.

can be found elsewhere [1,4]. Using these calculated sinograms, a simultaneous inverse Radon transform (SIRT) algorithm is applied. In this method, a reverse analysis [4] is carried out to recover both the local crystalline phase with the XRD sinograms and the local chemical–elemental composition with the XRF sinograms distributions. It is worth to note that both signals are two-dimensional depth-resolved. In this way, for each voxel related to a 3D spatial sample position, both the local powder-XRD pattern and local XRF spectrum are obtained. In Fig. 3e–l, XRD tomographic reconstructions for *slice1* (i-l) and *slice2* (e-h) are shown, with each image corresponding to a given diffracted intensity for a respective diffraction angle, as indicated in Fig. 3m.

A lattice parameter difference is observed between two LSCF regions of the two slices: one close to the outer edge the sample and the other one in the inner part of the LSCF

electrode. This can be observed through a qualitative comparison of the two tomographic results by inspecting and comparing Fig. 4g and k with h and l. One can note that the annular region affected by the sample free surface is around 3–5 μm thick. Rietveld refinements were performed on these two different regions, the one close to the surface ("*slice-out*") and the one in the core ("*slice-in*"). For both tomographic slices results, *slice1* and *slice2*, an average of the diffraction pattern was considered as follows: for *slice-out*, a surface layer of 5 μm thick was considered, and for *slice-in*, the core of the cylindrical sample about 5 μm far from the sample surface was considered. The perovskite $La_{0.6}Sr_{0.4}Co_{0.2}Fe_{0.8}O_3$ structure (ICSD database code number 187793) was identified and refined for both slices *slice1* and *slice2*; in total, four different regions were analysed: *slice1+slice-in*, *slice1+slice-out*, *slice2+slice-in* and *slice2+slice-out*. The results for the lattice parameters and unit cell volumes are plotted in Fig. 5b–d. A bigger unit cell volume is observed for *slice-out*, for both slices. This result confirms the qualitative observations of the XRD cartographies (Fig. 4g and k with h and l). This phenomenon could be due to either sample preparation and/or stress relaxation on the free surface.

Average diffraction patterns over line scans parallel to the internal sample interfaces were considered, which are shown in Fig. 5a. Rietveld analysis has also been performed on the XRD patterns obtained through the 2D raster scan. The results for the LSCF lattice parameters and unit cell volumes coming from the Rietveld analysis of the XRD patterns shown in Fig. 5a are also plotted in Fig. 5b–d. Small variations in the unit cell volume is observed, with a bigger volume observed close to the LSCF/Pt interface; which may be associated with small differences in particle sizes [16], and/or small differences in stoichiometry and oxidation state [10,41,44].

Similarly to the XRD analysis shown in Fig. 5a–d, a XRF analysis was also performed for the experiment at 18.15 keV. The XRF cartographies were also averaged over lines scans parallel to the LSCF/CGO interface. The integrated intensity is plotted in Fig. 5e as a function of the Y axis (see system of coordinates in Fig. 1). Each averaged line scan, shown in Fig. 5e, was analysed using PyMCA, and the isolated elements XRF intensities were deconvolved. The XRF intensity profiles of some selected elements are plotted in Fig. 5f–h.

Through both the 2D scanning projections, a few small crystalline inclusions into the LSCF layer are found, which can be seen by inspecting some selected Bragg reflections, as shown in Fig. 4b. The inclusions are evidenced by observing Fig. 4f and j, obtained through μXRD tomography, since this method allows to deconvolve the spatially resolved powder XRD pattern; analysing these obtained local pattern, a good matching for the crystalline structure of these inclusions is

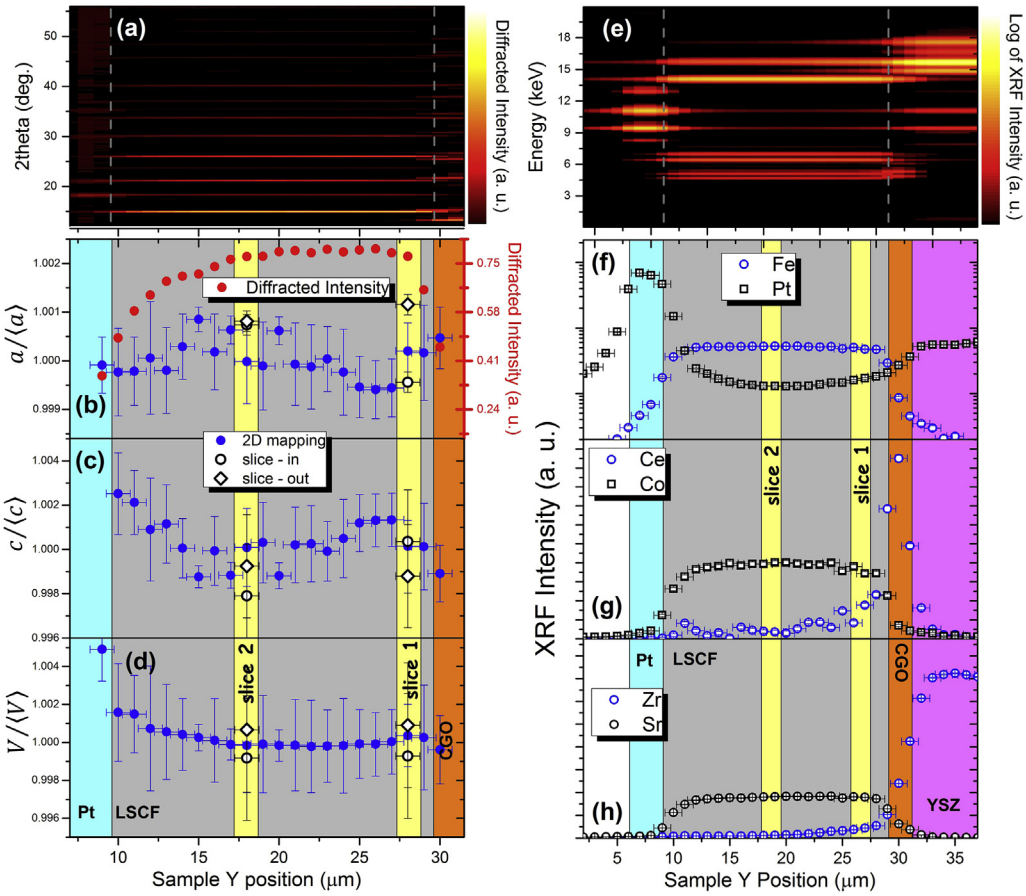

Fig. 5 – (a) Average diffraction patterns over line scans parallel to the internal sample interfaces. The results for the (b–c) lattice parameters and (d) unit cell volumes at sample depths. (e) Average XRF intensity over line scans parallel to the internal sample interfaces. (f–h) The XRF intensity profiles of some selected elements.

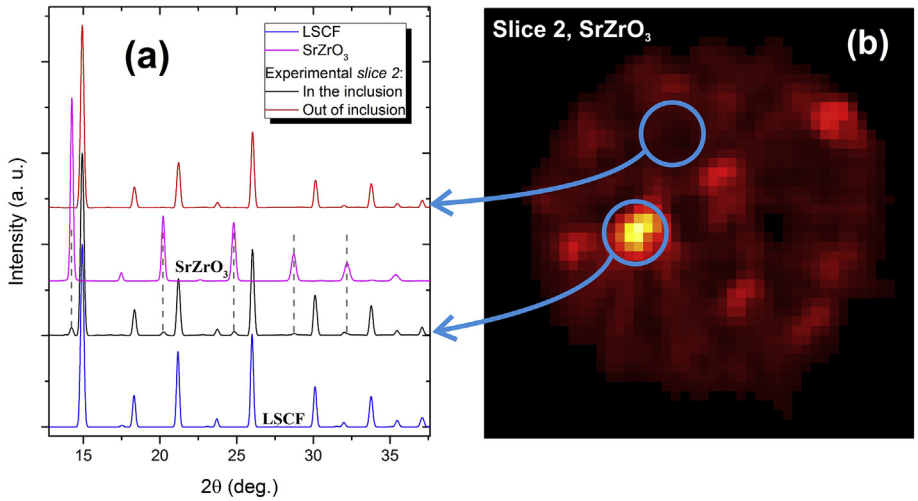

Fig. 6 – (a) Comparison between powder-XRD patterns: two experimental ones obtained from the *slice2* reconstructed slice (in the inclusion in black, and out of $SrZrO_3$ in red), and, calculated ones of $SrZrO_3$ (in magenta) and LSCF (in blue). (b) Same image shown in Fig. 3f; in detail, the regions where the two experimental XRD patterns were averaged. (For interpretation of the references to colour in this figure legend, the reader is referred to the web version of this article.)

obtained by considering the perovskite $SrZrO_3$ structure (ICSD database code number 29153). In Fig. 6a, two experimental XRD patterns obtained from the reconstructed *slice2* are compared, both averaged over 10 voxels; one is averaged over the region corresponding to a $SrZrO_3$ inclusion, and the other one is over a corresponding region without any $SrZrO_3$ signal. These two regions are respectively indicated in Fig. 6b, which is a reconstruction corresponding to the (121) reflection of $SrZrO_3$. In Fig. 6a, the presence of the oxide $SrZrO_3$ is evidenced by comparing the two experimental powder-XRD patterns with the calculated ones of $SrZrO_3$ and LSCF. The same matching is obtained for the inclusions observed in both the *slice1* and 2D scanning results.

The $SrZrO_3$ compound is one of the phases that are expected to be formed after a long term cell operation [33] (the CGO barrier interlayer limits but does not totally prevents the Zr or Sr diffusion). Significant Sr diffusion from LSCF to the CGO/YSZ interface [17,23] may form $SrZrO_3$ also at the CGO/YSZ interface. In order to examine this phenomenon, two-dimensional XRD cartographies of the different diffracted angle intensities related to CGO, $SrZrO_3$ and YSZ have been analysed around the region of the LSCF/CGO and CGO/YSZ interfaces (Fig. 7a–c, respectively). It is important to point out that the measured two-dimensional XRD patterns of the YSZ electrolyte did not result in powder-XRD like patterns; the corresponding scanned YSZ area present grain sizes of about a few microns in size. For this reason a precise phase identification of this phase is difficult. Nevertheless, the formation of SrZrO3 is clearly identified on Fig. 7b in the region of the CGO barrier layer.

In Fig. 8a is shown a magnified SEM image (backscattered electrons detected) of the LSCF/CGO (2 μm thick)/YSZ interfaces region, where, in addition to these layers which can be easily identified in this figure, also another layer can be resolved, with a slightly higher electron scattering signal in comparison with YSZ. A good matching of the spatial location of this extra identified layer is observed when compared to the so called "YSZ" intensity profile, shown in Fig. 8b, which may indicate a formation of a $(YSZ)_{1-x}(CeO_2)_x$ system in between the 8YSZ and CGO. We suspect that diffusion of CeO_2 may

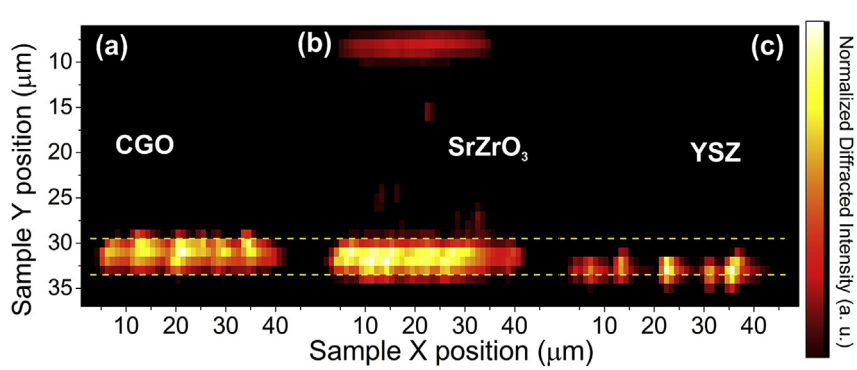

Fig. 7 – (a–c) XRD cartographies obtained from different diffracted angle intensities are plotted, which are indicated in the diffractogram in Fig. 3 as CGO, $SrZrO_3$ and YSZ, respectively.

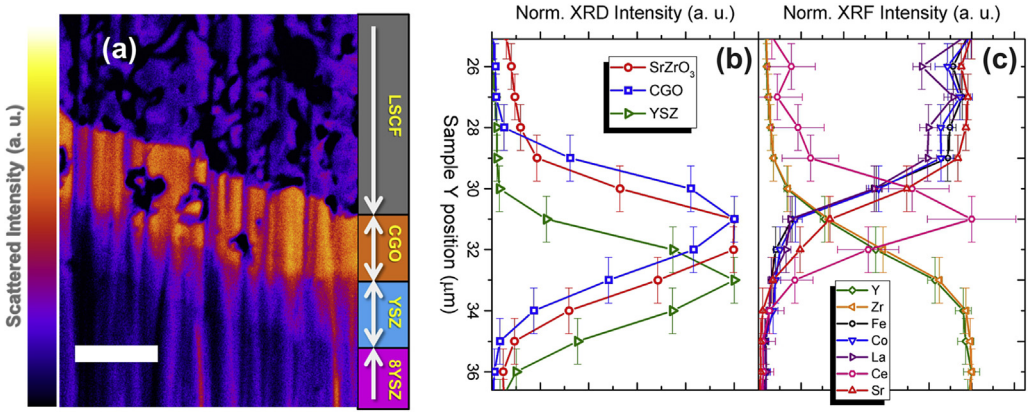

Fig. 8 – (a) SEM image of the indicated area with the red rectangle in Fig. 1; the scale bar is 2 μm. (b) Average intensity profiles along the LSCF/CGO/YSZ interfaces region for CGO, $SrZrO_3$ and YSZ taken from Fig. 7a–c, and (c) the XRF intensity profiles of some selected elements also along the LSCF/CGO/YSZ interfaces region.

occur during the sintering process and may lead to a the expansion of the YSZ unit cell volume by forming the $(YSZ)_{1-x}(CeO_2)_x$ system, which can assume the cubic, tetragonal or monoclinic crystalline phases [18,24]. Further investigations are needed for a precisely phase identification; especially because such phase transformation may affect the YSZ ionic conductivity and undermine the SOFC properties and lifetime.

Also, by inspecting the XRF signal of the four LSCF elements (shown in Fig. 8c), Fe, Co, Sr and La, a shift of the Sr edge towards the CGO layer is observed by comparing to the other three selected LSCF elements. In addition to this information, the (121) $SrZrO_3$ peak position is observed to be in between of the CGO and YSZ positions, as shown in Figs. 7a–c and 8b, which indicates the formation of the $SrZrO_3$ oxide in the CGO/YSZ interface.

Conclusions

The $SrZrO_3$ compound is one of the phases which are expected to be formed after the long term cell operation. Nevertheless, it is important to check if the phase can be detected in the pristine cell, since this phase is also likable to appear during the electrode sintering. In this work we demonstrate the capability 2D and 3D μbeam X-ray analysis, namely μXRD and μXRF, to investigate minor nano-crystalline phase inclusions, in the micrometre range, inside of a homogeneous nano-crystaline sample with tens of micrometres in size. In the present study, the technique has been used to detect the $SrZrO_3$ oxide as the crystalline inhomogeneity, and LSCF as the homogeneous material. It is important to point out that the detected 2D diffraction pattern of both of these compounds were identified as powder-like diffraction patterns; considering that the used beam spot size was of about 1 μm^2 of cross section, the grains of both of these compounds present less than 100 nm in size. This characteristic allowed to retrieve the local azimuthal integrated diffraction powder diffraction pattern through the tomographic reconstructions. Due to the mixed powder and monocrystalline diffraction patterns, in the YSZ/CGO interface region, the precise identification of the local YSZ phase transformations and also of minor nano-crystalline phases is more difficult. In this case, a combination of powder μXRD and white beam μLaue [37] tomographies could provide a more complete picture of the local micro-structure. Even though, thanks to the combined μXRD and μXRF analysis, the $SrZrO_3$ formation was identified in the YSZ/CGO interface. The present results open new perspectives in SOFC investigations, such as the investigation of real SOFCs submitted at different long term ageing processes, and correlate their micro-structural properties with different synthesis parameters.

Acknowledgements

The authors acknowledge access to the nanocharacterization platform (PFNC) at the Minatec Campus (CEA, Grenoble, France). We acknowledge the microXAS beamline at the SLS (Swiss Light Source, Paul Scherrer Institut, Villigen, Switzerland) for the high-quality beamtime and infrastructure necessary to perform our synchrotron-based investigation. We also acknowledge support of the Scientific Center for Optical and Electron Microscopy ScopeM of the Swiss Federal Institute of Technology ETHZ.

The research leading to these results has received funding from the European Union's Seventh Framework Programme (FP7/2007-2013) Fuel Cells and Hydrogen Joint Undertaking (FCH-JU-2013-1) under grant agreement No 621173.

REFERENCES

[1] Ávarez-Murga M, Bleuet P, Hodeau JL. Diffraction/scattering computed tomography for three-dimensional characterization of multi-phase crystalline and amorphous materials. J Appl Crystallogr 2012;45(6):1109–24. http://dx.doi.org/10.1107/S0021889812041039.

[2] Beale AM, Jacques SDM, Gibson EK, Di Michiel M. Progress towards five dimensional diffraction imaging of functional materials under process conditions. Coord Chem Rev

2014;277–278:208–23. http://dx.doi.org/10.1016/j.ccr.2014.05.008.
[3] Benito P, Monti M, De Nolf W, Nuyts G, Janssen G, Fornasari G, et al. Improvement in the coating homogeneity in electrosynthesized Rh structured catalysts for the partial oxidation of methane. Catal Today 2015;246:154–64. http://dx.doi.org/10.1016/j.cattod.2014.10.003.
[4] Bleuet P, Welcomme E, Dooryhée E, Susini J, Hodeau J-L, Walter P. Probing the structure of heterogeneous diluted materials by diffraction tomography. Nat Mater 2008;7(6):468–72. http://dx.doi.org/10.1038/nmat2168.
[5] Bleuet P, Audoit G, Barnes JP, Bertheau J, Dabin Y, Dansas H, et al. Specifications for hard condensed matter specimens for three-dimensional high-resolution tomographies. Microsc Microanal 2013;19(3):726–39.
[6] Chen Y, Yang L, Ren F, An K. Visualizing the structural evolution of LSM/xYSZ composite cathodes for SOFC by in-situ neutron diffraction. Sci Rep 2014;4:5179. http://dx.doi.org/10.1038/srep05179.
[7] Choi JJ, Park DS, Seong BG, Bae HY. Low-temperature preparation of dense $(Gd,Ce)O_{2-\delta}$–Gd_2O_3 composite buffer layer by aerosol deposition for YSZ electrolyte-based SOFC. Int J Hydrogen Energy 2012;37(12):9809–15. http://dx.doi.org/10.1016/j.ijhydene.2012.03.148.
[8] Delette G, Laurencin J, Usseglio-Viretta F, Villanova J, Bleuet P, Lay-Grindler E, et al. Thermo-elastic properties of SOFC/SOEC electrode materials determined from three-dimensional microstructural reconstructions. Int J Hydrogen Energy 2013;38(28):12379–91. http://dx.doi.org/10.1016/j.ijhydene.2013.07.027.
[9] Digiuseppe G, Sun L. Electrochemical performance of a solid oxide fuel cell with an LSCF cathode under different oxygen concentrations. Int J Hydrogen Energy 2011;36(8):5076–87. http://dx.doi.org/10.1016/j.ijhydene.2011.01.017.
[10] Ding H, Virkar AV, Liu F. Defect configuration and phase stability of cubic versus tetragonal yttria-stabilized zirconia. Solid State Ion 2012;215:16–23, http://doi.org/10.1016/j.ssi.2012.03.014. http://dx.doi.org/10.1016/j.ssi.2012.03.014.
[11] Endler-Schuck C, Leonide A, Weber A, Uhlenbruck S, Tietz F, Ivers-Tiffée E. Performance analysis of mixed ionic-electronic conducting cathodes in anode supported cells. J Power Sources 2011;196(17):7257–62. http://dx.doi.org/10.1016/j.jpowsour.2010.11.079.
[12] Endler-Schuck C, Joos J, Niedrig C, Weber A, Ivers-Tiffée E. The chemical oxygen surface exchange and bulk diffusion coefficient determined by impedance spectroscopy of porous $La_{0.58}Sr_{0.4}Co_{0.2}Fe_{0.8}O_{3-\delta}$ (LSCF) cathodes. Solid State Ionics 2015;269:67–79. http://dx.doi.org/10.1016/j.ssi.2014.11.018.
[13] European SOFC-Life Project. Fuel Cells Bull 2014;2014(5):11.
[14] Fergus JW. Electrolytes for solid oxide fuel cells. J Power Sources 2006;162(1):30–40. http://dx.doi.org/10.1016/j.jpowsour.2006.06.062.
[15] Ghouse M, Al-Yousef Y, Al-Musa A, Al-Otaibi MF. Preparation of $La_{0.6}Sr_{0.4}Co_{0.2}Fe_{0.8}O_3$ nanoceramic cathode powders for solid oxide fuel cell (SOFC) application. Int J Hydrogen Energy 2010;35(17):9411–9. http://dx.doi.org/10.1016/j.ijhydene.2010.04.144.
[16] Haider MA, Capizzi AJ, Murayama M, McIntosh S. Reverse micelle synthesis of perovskite oxide nanoparticles. Solid State Ionics 2011;196(1):65–72. http://dx.doi.org/10.1016/j.ssi.2011.06.013.
[17] Hardy JS, Templeton JW, Edwards DJ, Lu Z, Stevenson JW. Lattice expansion of LSCF-6428 cathodes measured by in situ XRD during SOFC operation. J Power Sources 2012;198(0):76–82. http://dx.doi.org/10.1016/j.jpowsour.2011.09.099.
[18] Hunter BA, Howard CJ, Kim D-J. Neutron diffraction study of tetragonal zirconias containing tetravalent dopants. Aust J Phys 1998;51:539–45. http://dx.doi.org/10.1071/P97060.
[19] Inaba H, Tagawa H. Ceria-based solid electrolytes. Solid State Ion 1996;83(1–2):1–16. http://dx.doi.org/10.1016/0167-2738(95)00229-4.
[20] Jo KH, Kim JH, Kim KM, Lee IS, Kim SJ. Development of a new cost effective Fe-Cr ferritic stainless steel for SOFC interconnect. Int J Hydrogen Energy 2015;40(30):9523–9. http://dx.doi.org/10.1016/j.ijhydene.2015.05.125.
[21] Jordan N, Assenmacher W, Uhlenbruck S, Haanappel VAC, Buchkremer HP, Stover D, et al. $Ce_{(0.8)}Gd_{(0.2)}$ $O_{(2\text{-delta})}$ protecting layers manufactured by physical vapor deposition for IT-SOFC. Solid State Ionics 2008;179(21–26):919–23. http://dx.doi.org/10.1016/j.ssi.2007.12.008.
[22] Jun Ko H, Myung J, Lee J, Hyun S, Chung JS. Synthesis and evaluation of $(La_{0.6}Sr_{0.4})(Co_{0.2}Fe_{0.8})O_3$ (LSCF) - $Y_{0.08}Zr_{0.92}O_{1.96}$ (YSZ) - $Gd_{0.1}Ce_{0.9}O_{2\text{-}d}$ (GDC) dual composite SOFC cathodes for high performance and durability. Int J Hydrogen Energy 2012;37(22). http://dx.doi.org/10.1016/j.ijhydene.2012.08.099. 17209–12216.
[23] Kiebach R, Zhang W-W, Zhang W, Chen M, Norrman K, Wang H-J, et al. Stability of $La_{0.6}Sr_{0.4}Co_{0.2}Fe_{0.8}O_3/Ce_{0.9}Gd_{0.1}O_2$ cathodes during sintering and solid oxide fuel cell operation. J Power Sources 2015;283:151–61. http://dx.doi.org/10.1016/j.jpowsour.2015.02.064.
[24] Kountouros P, Petzow G. In: Badwal SPS, Bannister MJ, Hannink RHJ, editors. Science and technology of Zirconia V. Lancaster, PA, VSA: Technomic Publishing; 1993.
[25] Laurencin J, Delette G, Lefebvre-Joud F, Dupeux M. A numerical tool to estimate SOFC mechanical degradation: case of the planar cell configuration. J Eur Ceram Soc 2008;28(9):1857–69. http://dx.doi.org/10.1016/j.jeurceramsoc.2007.12.025.
[26] Laurencin J, Hubert M, Couturier K, L. Bihan T, Cloetens P, Lefebvre-Joud F, et al. Reactive mechanisms of LSCF single-phase and LSCF-CGO composite electrodes operated in anodic and cathodic polarisations. Electrochim Acta 2015;174:1299–316. http://dx.doi.org/10.1016/j.electacta.2015.06.080.
[27] Leng YJ, Chan SH, Khor KA, Jiang SP. Development of LSM/YSZ composite cathode for anode-supported solid oxide fuel cells. J Appl Electrochem 2004;34:409–15.
[28] Lind OC, De Nolf W, Janssens K, Salbu B. Micro-analytical characterisation of radioactive heterogeneities in samples from Central Asian TENORM sites. J Environ Radioact 2013;123:63–70. http://dx.doi.org/10.1016/j.jenvrad.2012.02.012.
[29] Liu Y, Chen K, Zhao L, Chi B, Pu J, Jiang SP, et al. Performance stability and degradation mechanism of $La_{0.6}Sr_{0.4}Co_{0.2}Fe_{0.8}O_{3-\delta}$ cathodes under solid oxide fuel cells operation conditions. Int J Hydrogen Energy 2014;39(28):15868–76. http://dx.doi.org/10.1016/j.ijhydene.2014.03.077.
[30] Mahato N, Banerjee A, Gupta A, Omar S, Balani K. Progress in material selection for solid oxide fuel cell technology: a review. Prog Mater Sci 2015;72:141–337. http://dx.doi.org/10.1016/j.pmatsci.2015.01.001.
[31] Mai A, Haanappel VAC, Uhlenbruck S, Tietz F, Stöver D. Ferrite-based perovskites as cathode materials for anode-supported solid oxide fuel cells: part I. Variation of composition. Solid State Ionics 2005;176(15–16):1341–50. http://dx.doi.org/10.1016/j.ssi.2005.03.009.
[32] Mai A, Becker M, Assenmacher W, Tietz F, Hathiramani D, Ivers-Tiffée E, et al. Time-dependent performance of mixed-conducting SOFC cathodes. Solid State Ionics 2006;177(19–25 SPEC. ISS.):1965–8. http://dx.doi.org/10.1016/j.ssi.2006.06.021.

[33] Ni DW, Esposito V. Densification of $Ce_{0.9}Gd_{0.1}O_{1.95}$ barrier layer by in-situ solid state reaction. J Power Sources 2014;266:393–400. http://dx.doi.org/10.1016/j.jpowsour.2014.05.044.
[34] De Nolf W, Janssens K. Micro X-ray diffraction and fluorescence tomography for the study of multilayered automotive paints. Surf Interface Anal 2010;42:411–8. http://dx.doi.org/10.1002/sia.3125.
[35] Oh M-Y, Unemoto A, Amezawa K, Kawada T. Stability of $La_{0.6}Sr_{0.4}Co_{0.2}Fe_{0.8}O_{3\text{-delta}}$ as SOFC Cathode. J Electrochem Soc 2012;159(10):F659–64. http://dx.doi.org/10.1149/2.063210jes.
[36] Park SY, Ahn JH, Jeong CW, Na CW, Song RH, Lee JH. Ni-YSZ-supported tubular solid oxide fuel cells with GDC interlayer between YSZ electrolyte and LSCF cathode. Int J Hydrogen Energy 2014;39(24):12894–903. http://dx.doi.org/10.1016/j.ijhydene.2014.06.103.
[37] Ferreira Sanchez D, Villanova J, Laurencin J, Micha J-S, Montani A, Gergaud P, et al. X-ray micro Laue diffraction tomography analysis of a solid oxide fuel cell. J Appl Crystallogr 2015;48(2):357–64. http://dx.doi.org/10.1107/S1600576715002447.
[38] Shearing PR, Gelb J, Brandon NP. X-ray nano computerised tomography of SOFC electrodes using a focused ion beam sample-preparation technique. J Eur Ceram Soc 2010;30(8):1809–14. http://dx.doi.org/10.1016/j.jeurceramsoc.2010.02.004.
[39] Shearing PR, Golbert J, Chater RJ, Brandon NP. 3D reconstruction of SOFC anodes using a focused ion beam lift-out technique. Chem Eng Sci 2009;64(17):3928–33. http://dx.doi.org/10.1016/j.ces.2009.05.038.
[40] Shearing PR, Bradley RS, Gelb J, Tariq F, Withers PJ, Brandon NP. Exploring microstructural changes associated with oxidation in Ni–YSZ SOFC electrodes using high resolution X-ray computed tomography. Solid State Ionics 2012;216:69–72. http://dx.doi.org/10.1016/j.ssi.2011.10.015.
[41] Soldati AL, Baqué L, Napolitano F, Serquis A. Cobalt–iron red–ox behavior in nanostructured $La_{0.4}Sr_{0.6}Co_{0.8}Fe_{0.2}O_{3-\delta}$ cathodes. J Solid State Chem 2013;198:253–61. http://dx.doi.org/10.1016/j.jssc.2012.10.019.
[42] Solé VA, Papillon E, Cotte M, Walter P, Susini J. A multiplatform code for the analysis of energy-dispersive X-ray fluorescence spectra. Spectrochim Acta Part B At Spectrosc 2007;62(1):63–8. http://dx.doi.org/10.1016/j.sab.2006.12.002.
[43] Staniforth JZ, Evans SE, Good OJ, Darton RJ, Ormerod RM. A novel perovskite based catalyst with high selectivity and activity for partial oxidation of methane for fuel cell applications. Dalton Trans (Cambridge, England 2003) 2014;21(3):4–9. http://dx.doi.org/10.1039/c4dt01288g.
[44] Tai LW, Nasrallah MM, Anderson HU, Sparlin DM, Sehlin SR. Structure and electrical-properties of $La_{1\text{-}X}$ $Sr_xCo_{1\text{-}Y}$ Fe_yO_3. 1. The System $La_{0.8}Sr_{0.2}Co_{1\text{-}Y}$ Fe_yO_3. Solid State Ionics 1995;76(3–4):259–71. http://dx.doi.org/10.1016/0167-2738(94)00244-M.
[45] Wang W, Mogensen M. High-performance lanthanum-ferrite-based cathode for SOFC. Solid State Ionics 2005;176(5–6):457–62. http://dx.doi.org/10.1016/j.ssi.2004.09.007.
[46] Wilde V, Störmer H, Szasz J, Wankmüller F, Ivers-Tiffée E, Gerthsen D. Effect of $Gd_{0.2}Ce_{0.8}O_2$ sintering temperature on formation of a $SrZrO_3$ blocking layer between $Y_{0.16}Zr_{0.84}O_2$, $Gd_{0.2}Ce_{0.8}O_2$ and $La_{0.58}Sr_{0.4}Co_{0.2}Fe_{0.8}O_3$. ECS Trans 2015;66(2):103107.
[47] Yamamoto O. Solid oxide fuel cells: fundamental aspects and prospects. Electrochim Acta 2000;45(15–16):2423–35. http://dx.doi.org/10.1016/S0013-4686(00)00330-3.
[48] Yokokawa H, Tu H, Iwanschitz B, Mai A. Fundamental mechanisms limiting solid oxide fuel cell durability. J Power Sources 2008;182:400–12. http://dx.doi.org/10.1016/j.jpowsour.2008.02.016.
[49] Zhang-Steenwinkel Y, Yu Q, Van Berkel FPF, Van Tuel MMA, Rietveld B, Tu H. High performance solid-oxide fuel cell: opening windows to low temperature application. Int J Hydrogen Energy 2016;41(13):5824–32. http://dx.doi.org/10.1016/j.ijhydene.2016.02.033.